Chemical Engineering Science 172 (2017) 216–229

Contents lists available at ScienceDirect

Chemical Engineering Science

journal homepage: www.elsevier.com/locate/ces

Characteristics of liquid flow in a rotating packed bed for CO_2 capture: A CFD analysis

Peng Xie, Xuesong Lu, Xin Yang, Derek Ingham, Lin Ma *, Mohamed Pourkashanian

Energy2050, Mechanical Engineering, Faculty of Engineering, University of Sheffield, Sheffield S10 2TN, UK

HIGHLIGHTS

- A 2D CFD model is built using a fine grid to resolve the liquid flow in an RPB.
- The model predictions are in reasonable agreement with observations.
- On increasing the MEA concentration, the degree of liquid dispersion decreases.
- High rotational speed decreases the holdup and increases the liquid dispersion.
- At a high contact angle, more liquid droplets are formed but holdup decreases.

ARTICLE INFO

Article history:
Received 8 April 2017
Received in revised form 15 June 2017
Accepted 21 June 2017
Available online 23 June 2017

Keywords:
Rotating packed bed
CFD
Flow pattern
Liquid holdup
VOF model

ABSTRACT

Rotating packed beds (RPBs) have been proposed as an emerging technology to be used for post-combustion CO_2 capture (PCC) from the flue gas. However, due to the complex structure of the packing in RPBs, characteristics of the liquid flow within RPBs are very difficult to be fully investigated by experimental methods. Therefore, in this paper, a two-dimensional (2D) CFD model has been built for analysing the characteristics of liquid flow within an RPB. The volume of fluid (VOF) multiphase flow model is implemented to calculate the flow field and capture the interface between the gas and liquid phases in the RPB. The simulation results show good agreement with the experimental data. The distinct liquid flow patterns in different regions of an RPB are clearly observed. The simulation results indicate that increasing the rotational speed dramatically decreases the liquid holdup and increases the degree of the liquid dispersion. The increasing liquid jet velocity decreases the liquid residence time but slightly increases the liquid holdup. In addition, the liquid holdup increases and the degree of the liquid dispersion decreases with increasing MEA concentration, but the effects are weaker at a higher rotational speed. With the increasing of the contact angle, both the liquid holdup and the degree of the liquid dispersion are reduced. This proposed model leads to a much better understanding of the liquid flow characteristics within RPBs.

1. Introduction

The rotating packed bed (RPB), as a type of process intensification (PI) technology, was invented by Ramshaw and Mallinson (1981) for enhancing the gas–liquid mass transfer in chemical processes. A schematic diagram of a typical RPB is shown in Fig. 1. In the RPB, liquid flow is injected radially from the centre of the bed and it is split continuously into discrete liquid ligaments, thin films and tiny droplets by the rotating porous packing. This can dramatically increase the interfacial area and promotes intensive mixing and mass transfer between the liquid phase and the gas phase that flows through the RPB (Yan et al., 2014). Applications of RPB include such as separation process intensification (Chen and Liu, 2002; Chu et al., 2014), reaction process intensification (Chen et al., 2010), nanoparticles syntheses (Chen et al., 2000), etc. In recent years, in order to control the global CO_2 emission from the power generation sector, the RPB has been proposed as an emerging technology to be used for post-combustion CO_2 capture (PCC) from the flue gases (Cheng et al., 2013; Joel et al., 2014; Lin and Kuo, 2016; Wang et al., 2015; Zhao et al., 2014). It has the potential to significantly reduce the capital cost, improve the process dynamics and use high concentrated amine-based solvents, compared with using conventional packed columns (Wang et al., 2015). However, the fluid mechanics of the RPB is not fully understood, thus accurately predicting the characteristics of the liquid

* Corresponding author.
E-mail address: lin.ma@sheffield.ac.uk (L. Ma).

http://dx.doi.org/10.1016/j.ces.2017.06.040
0009-2509/

Nomenclature

A_{int}	gas-liquid interfacial area, m^2
d	width of the nozzle, m
I_d	liquid dispersion index, m^{-1}
k	the curvature of the interface
N	rotational speed, rpm
$\vec{n}$	unit normal vector
r	radial position in the RPB, m
$\bar{t}$	mean residence time, s
U	superficial flow velocity, m/s
u_0	liquid jet velocity, m/s
V	volume, m^3
v_r	relative velocity, m/s

Greek symbols

α	volume fraction
γ	contact angle, deg
ε_L	liquid holdup
μ	dynamic viscosity, Pa·s
ν	kinematic viscosity, m^2/s
ρ	density, kg/m^3
σ	surface tension coefficient, N/m
ω	rotational speed, rad/s

Subscripts

g	gas phase
l	liquid phase

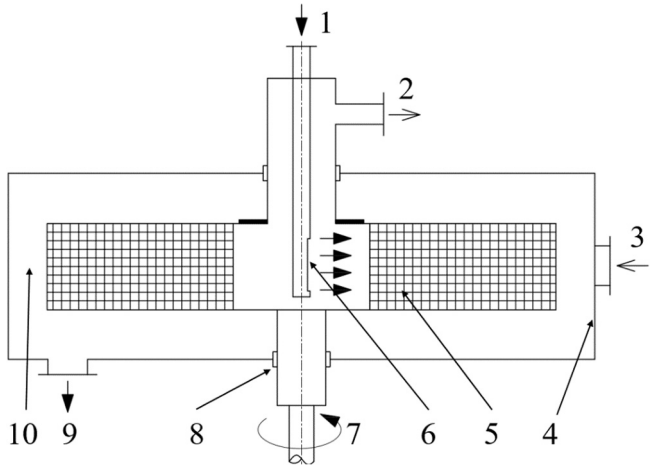

Fig. 1. Schematic diagram of a typical RPB with a counter-current flow arrangement (1. Liquid inlet; 2. Gas outlet; 3. Gas inlet; 4. Hull; 5. Packing; 6. Liquid distributor; 7. Rotating shaft; 8. Seal; 9. Liquid outlet; 10. Cavity zone).

solvent flow and subsequently the mass transfer within the RPB is difficult and it is critical for design and optimisation of the RPB for PCC applications.

Research on the mass transfer process in the RPB has been conducted continuously since the invention of the technology through both theoretical and experimental investigations. Different modelling methods, including theoretical and semi-empirical correlations (Jiao et al., 2010; Munjal et al., 1989; Tung and Mah, 1985), numerical simulations (Joel et al., 2015, 2014; Kang et al., 2014, 2016; Qian et al., 2009; Yang et al., 2016; Yi et al., 2009; Yu et al., 2016; Zhang et al., 2016) and artificial intelligence approaches (Saha, 2009; Zhao et al., 2014), etc. have been proposed. Since the mass transfer within the RPB is heavily influenced by the hydrodynamic characteristics of the liquid flow, such as the patterns of the flow, the amount of liquid holdup, the degree of the liquid dispersion, and the effective interfacial area for mass transfer to take place, a deep understanding of the liquid flow characteristics within RPBs is essential.

So far, different experimental methods have been employed to analyse the characteristics of the liquid flow in the RPB. For instance, Burns and Ramshaw (1996) and Guo et al. (2000) obtained the flow patterns in the packing region of RPBs experimentally by employing a fixed camera and a synchronously rotational video camera with the packing. It is generally believed that there are mainly three flow regimes in the bulk packing region of the RPB, i.e. the pore flow within the packing voids, the discrete droplet flow, and the film flow on the packing surface. Distinct liquid maldistribution is also observed. This indicates that the actual liquid flow within an RPB is very complex and far from being a uniform film flow, which was assumed in some existing mass transfer models for the RPB (Kumar and Rao, 1990; Munjal et al., 1989; Tung and Mah, 1985). Further, Guo et al. (2000) observed different flow patterns between the liquid entrance region and the bulk region of the packing. They have tried to measure the liquid film thickness on the packing surface of a model RPB. However, due to the image speed limitations of the video camera employed, liquid droplets and filaments were difficult to be distinguished from films in the stream across the voids. Yan et al. (2012) employed a trajectory tracking method to obtain the liquid flow characteristics in an RPB with random packing. They observed the dynamics of droplets in RPBs, such as droplet–droplet collisions, droplet-packing collisions, deformation and breakup of liquid droplets. This further confirmed the complexity of the flow and they affirmed that there is a certain proportion of turbulent flow even within the liquid film flow. However, this method is only suitable for random packings. Other experimental techniques, such as the visual experimental method have been developed by Guo et al. (2014) through observing the ink marks on paper tapes that were wrapped around the packing, to investigate the depth of the end-effect zone of the packing in an RPB.

A number of attempts have also be made to measure the liquid holdup in the RPBs. For example, Basic and Dudukovic (1995) and Burns et al. (2000) investigated the effects of the operating parameters on the liquid holdup by utilizing conductance measurements; Chen et al. (2004) determined the liquid holdup by measuring the amount of retained liquid in the RPB; and Yang et al. (2015a) employed an X-ray CT technique to examine the liquid distribution and liquid holdup in RPBs. Although experiments can obtain important information, through long experimental periods, constraints in the technology and expensive cost limit these methods from being extensively employed for engineering design.

With the development of CFD technology, CFD simulations have become a powerful tool to cover the shortage of experimental researches on the chemical equipment. On the one hand, CFD can visually present some detailed flow characteristics on the internals of the chemical equipment, which is often difficult to obtain through experimental measurements (Liu et al., 2017). One the other hand, CFD can be used to perform "virtual experiments" under different conditions for obtaining data, which is faster and

more economical than experimental methods (Raynal and Royon-Lebeaud, 2007). However, due to the difficulties that arise from the complex packing structure, the rotational motion and the multi-scale flow characteristics, only a few CFD simulations of the RPB have been conducted until now. For instance, Llerena-Chavez and Larachi (2009) and Yang et al. (2015b) simulated the single gas phase flow in RPBs using three-dimensional (3D) porous media models and the dry pressure drop and gas flow maldistribution in the RPB were investigated. However, without resolving the packing geometry in the simulation, it is very difficult to obtain the detailed information on the gas flow that is influenced by the structure of the packing. As an improvement, Yang et al. (2010) and Liu et al. (2017) simulated the single phase flow using the 3D wire mesh geometry models, which give a better understanding of the gas flow in the RPB. However, the significant behaviour of the discrete liquid is not considered in these CFD simulations.

Recently, the Volume of Fluid (VOF) multiphase flow model has demonstrated the ability to simulate the behaviour of the discrete liquid by tracking the gas-liquid interface (Gao et al., 2015; Nikolopoulos et al., 2009) and it has been employed to investigate the gas-liquid two-phase flow in RPBs (Guo et al., 2016; Shi et al., 2013; Yang et al., 2016). However, limited by computational resources, it is presently impossible to run simulations both taking into account the time-dependent gas–liquid interaction and the real geometry of the packing in a detailed 3D model. Therefore, 2D models have been used based on some geometric simplifications. For example, Shi et al. (2013) employed a 2D VOF model to analysis the liquid flow characteristics within an RPB. Further, Guo et al. (2016) employed a VOF-based method and based on the geometry model of Shi et al. (2013) to investigate the micromixing efficiency in the RPB. In these models (Guo et al., 2016; Shi et al., 2013), only the liquid droplets can be observed in the RPB, which is far different from the observed flow patterns in the experiments (Burns and Ramshaw, 1996; Guo et al., 2000). This is due to the computational grid in the vicinity of the packing surface is not small enough to capture the thin liquid films. Yang et al. (2016) employed the VOF model to analyse the vacuum deaeration process in RPBs. However, due to the coarse computational grids, the gas-liquid interface is difficult to be accurately captured in the RPB and the liquid was assumed to be evenly fed into the packing with a very small velocity in the inner periphery of the RPB rotor, which is very different from the real conditions. In addition, in the aforementioned VOF-based CFD models (Guo et al., 2016; Shi et al., 2013; Yang et al., 2016), all the wires used in the wire mesh packing are assumed to have square cross-sections which is mainly for reducing the difficulty of generating the computational grids. However, in reality, wire meshes having a round cross-section are the most common packing materials. For the wires that directly knock and split the liquid, the cross-section shape has a great influence on the liquid flow characteristics in the RPB. In summary, it is difficult to obtain a detailed and accurate prediction of the liquid flow characteristics in an RPB by the existing CFD models of RPBs.

In order to achieve a more reliable prediction of the liquid flow characteristics in an RPB, a new 2D computational framework of an RPB is built based on the VOF method. This model adopts the real round cross-section of the wire mesh as the packing characteristics and a non-uniform grid generation strategy has been employed to make the model available to capture the liquid films on the packing surface so that both the formation of the liquid droplet and the formation of the liquid film can be simulated. In addition, the fluid flow is calculated in a rotational coordinate system that is fixed on the RPB rotor. The SST k-ω model is applied to close the Navier-Stokes equations. Both low and high concentrations of aqueous monoethanolamine (MEA) solutions are investigated for the possible flow patterns in the RPB. The effects of the rotational speed, liquid jet velocity, liquid viscosity and contact angle have been simulated to provide and improve the understanding on the detailed flow patterns, liquid holdup, liquid residence time, and the degree of liquid dispersion, which are important parameters for RPB designs.

2. CFD model

2.1. Geometry of the RPB

The RPB simulated is based on the experiments of Yang et al. (2015a), and Fig. 2(a) shows the main dimensions of the packed bed. It has a 20 mm height, 42 mm inner diameter and 82 mm outer diameter, and the specific area is 497 m^2/m^3 and the void fraction is 0.95. The liquid is radially injected into the packing from the centre of the RPB through a liquid distributor, which is designed as a rectangular crack with the size of 1 mm × 15 mm. Both the wire mesh packing and nickel foam packing were investigated experimentally. However, only the wire mesh packing is selected to be investigated in this paper. The wire mesh packing has a better performance to deal with the high viscosity fluid than the nickel foam packing (Yang et al., 2015a) and it has a good mass transfer performance among several different types of packings (Chen et al., 2006). In addition, it is suitable to deal with large amounts of flue gas in the PCC process due to the high porosity. The rotational speed of the bed varied from 500 rpm to 2500 rpm, the liquid flow rate ranges from 1094 ml/s to 2580 ml/s, and this means that the liquid jet velocity ranges from 1.22 m/s to 2.87 m/s. The data on the liquid holdup under these operating conditionals are available from the experiment (Yang et al., 2015a).

Because of the irregular structure and limited information on the packing employed in the experiments (Yang et al., 2015a), it is almost impossible to make an identical packing arrangement in the CFD model. The annular packing region of the RPB consists of a woven wire mesh in rolls, which can be reasonably simplified into a concentric multi-layer wire mesh, and each layer is composed of concentric and coaxial wires (see Fig. 2(a)). A cross-section, where there are only coaxial wires, is chosen to build up the 2D calculation domain (see Fig. 2(b)). The influence of the concentric wires on the liquid flow has to be ignored, mainly because in a 2D model the concentric wires would form closed circles that the liquid cannot flow across. Since the direction of the liquid flow in most of the packing region is almost radial relative to the packing, it is expected that the liquid flow characteristics would be similar to that when it hits a coaxial wire.

In order to make the 2D model have similar characteristics, such as void fraction and specific area, compared to the real physical models, several important parameters have been controlled to generate the 2D packing geometry. The diameter of the wires is 0.5 mm and the distance between the centres of two adjacent packing wires in the circumferential direction is 3.5 mm. There are 21 concentric packing layers in total and the distance between the centres of two adjacent mesh layers in the radial direction is 1 mm. Under this arrangement, the void fraction of the packing is 0.94, and the specific area is 469 m^{-1}. These parameters are similar to the RPB employed by Yang et al. (2015a). Therefore, the simulation results of the liquid holdup can be compared with the experimental results for model validation.

2.2. Computational grid

The computational grid generation is a critical step that influences the convergence, stability, and accuracy of the simulations. From the previous study (Burns and Ramshaw, 1996; Guo et al., 2000; Yan et al., 2014), the liquid film flow is an essential flow

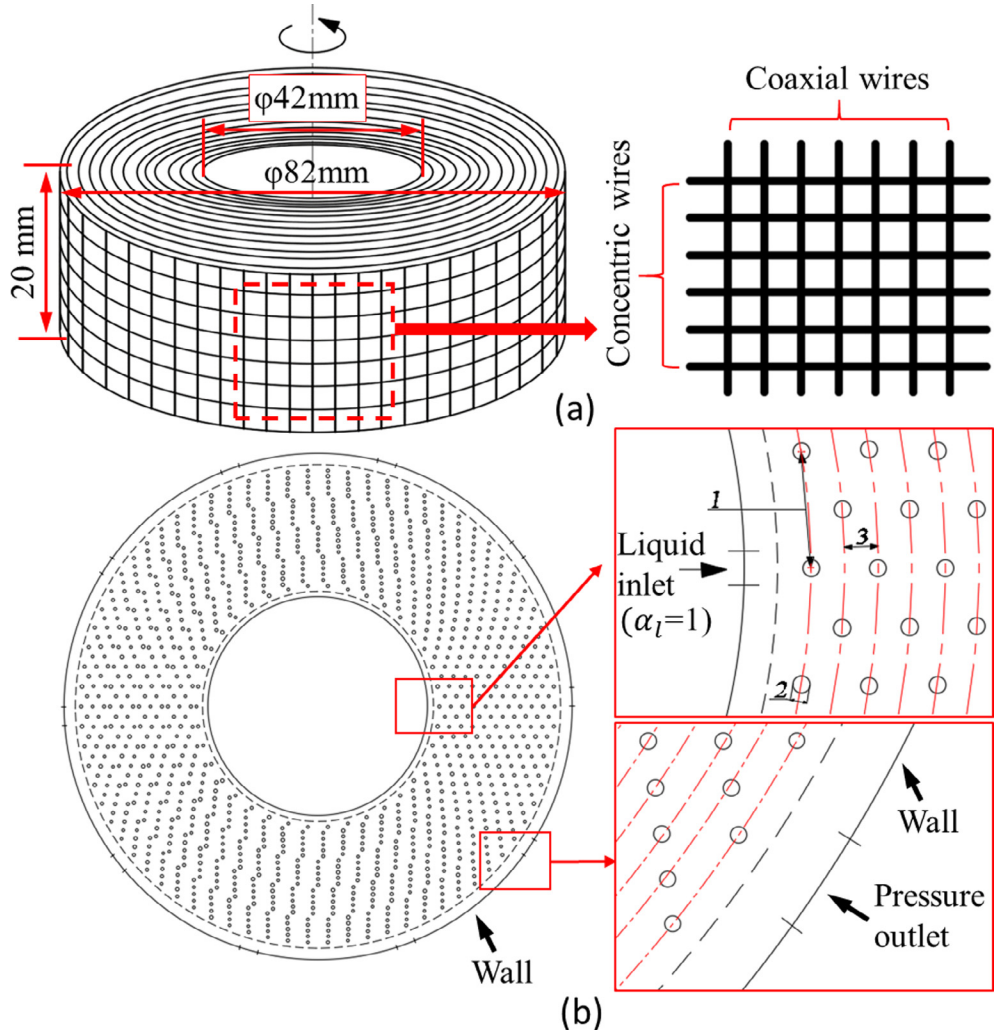

Fig. 2. (a) Schematic diagram of the wire mesh packing; and (b) 2D calculation domain of an RPB and the partial schematic illustration of the packing arrangement and boundary conditions (1. Center distance between two adjacent wires in the circumferential direction; 2. Diameter of the wire; 3. Center distance between two adjacent mesh layers).

pattern in the RPB. Moreover, the morphology of small ligaments and droplets is very sensitive to the boundary layers on the packing surfaces. Accurately resolving the boundary layer in the neighbourhood of the packing surfaces is the basis for accurately predicting the liquid flow field by using the VOF-based CFD methods. Therefore, considering the computational accuracy of the liquid flow field, especially in the vicinity of the packing surfaces, as well as the overall computing efficiency, the flow domain is discretized with a non-uniform mesh as shown in Fig. 3. A higher mesh density is implemented near the packing surface in order to resolve the flow boundary layer accurately and then the size of the grids grows gradually. In the region far away from the packing surface, the grid is quadrilateral dominate. The final grid size is a result of a grid sensitivity study, which is discussed in more detail in Section 2.7. In this paper, the geometry and grid of the computational domain is generated with ICEM CFD 16.1.

2.3. Mathematical model

The simulations are performed based on the following assumptions: (i) The gas and liquid fluids are Newtonian and incompressible with no phase change. (ii) The system is under isothermal condition and the flow is time-dependent. (iii) The surface tension is constant and uniform at the interface between the two fluids. The VOF method, proposed by Hirt and Nichols (1981), and the level-set method, proposed by Osher and Sethian (1988) are two popular surface-tracking techniques that are used when the tracking of the interface is of much interest. However, the level-set method has a deficiency in the volume or mass non-conservation in the under-resolved regions during the calculation while the VOF method is naturally volume-conserved (ANSYS Inc, 2015). In addition, the coupled level-set and VOF approach has been provided in ANSYS Fluent, however, when adopting this method, the convergence of the continuity equation becomes more difficult than when adopting the VOF method. Therefore, the VOF method is adopted in this paper. In the VOF model, a single set of momentum equations are shared by the two fluids, and the volume fraction of each of the fluids in each computational cell is tracked throughout the domain.

When solving for the flow within the RPB, it is advantageous to employ a moving reference frame that is fixed on the RPB rotor where the packing remains stationary when viewed from the reference frame, and this makes it easier to analyse the time-sequenced microcosmic liquid transformation process in the RPB. The governing equations of fluid flows in the rotational moving reference frame can be written as follows:

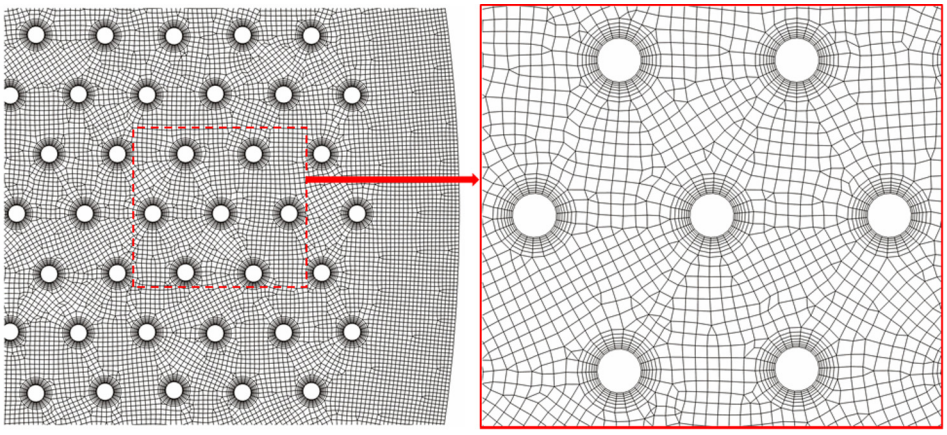

Fig. 3. Computational grid arrangement in the RPB.

The continuous equation

$$\frac{\partial \rho}{\partial t} + \nabla \cdot (\rho \vec{v}_r) = 0 \tag{1}$$

The momentum conservation equation

$$\frac{\partial}{\partial t}(\rho \vec{v}_r) + \nabla \cdot (\rho \vec{v}_r \vec{v}_r) + \rho(2\vec{\omega} \times \vec{v}_r + \vec{\omega} \times \vec{\omega} \times \vec{r}) = -\nabla p + \nabla \cdot [\mu(\nabla \vec{v}_r + \nabla \vec{v}_r^T)] + \vec{F}_{vol} \tag{2}$$

where $(2\vec{\omega} \times \vec{v}_r)$ and $(\vec{\omega} \times \vec{\omega} \times \vec{r})$ stand for the Coriolis acceleration and the centripetal acceleration, respectively.

The volume fraction equation

$$\frac{\partial}{\partial t}(\alpha_l \rho_l) + \nabla \cdot (\alpha_l \rho_l \vec{v}_{lr}) = 0 \tag{3}$$

where l represents the liquid phase, t is the time, α_l is the volume fraction for liquid phase, and $\vec{v}_{lr}$ is the relative velocity for liquid phase.

The volume fraction of the gas phase is calculated based on the following constraint:

$$\alpha_g = 1 - \alpha_l \tag{4}$$

When the value α_l of a computational cell is equal to zero, it indicates that the cell is full of gas phase, when $\alpha_l = 1$, it means the cell is full of liquid, when $0 < \alpha_l < 1$, the cell contains the gas-liquid interface. The interface is reconstructed by the Geometric-Reconstruction scheme (Youngs, 1982), which uses a piecewise-linear approach to represent the interface between the fluids.

The fluid properties, such as density ρ and dynamic viscosity μ, take volume-averaged values as follows:

$$\rho = \alpha_l \rho_l + (1 - \alpha_l)\rho_g \tag{5}$$

$$\mu = \alpha_l \mu_l + (1 - \alpha_l)\mu_g \tag{6}$$

The surface tension has a significant impact on the liquid dispersion. The current work employs the CSF (Continuum Surface Force) model proposed by Brackbill et al. (1992) to account for the effect of the surface tension, i.e. the surface tension force is transformed to a volume force source term F_{vol} in the momentum equations. The localised volume force F_{vol} can be estimated using the following relationship:

$$F_{vol} = \sigma \frac{\rho k \nabla \alpha_l}{0.5(\rho_l + \rho_g)} \tag{7}$$

where σ is the surface tension coefficient, k is the gas-liquid interface curvature and it is defined in terms of the divergence of the unit normal ñ and it is given as

$$k = \nabla \cdot \tilde{n} \tag{8}$$

where $\tilde{n} = n/|n|$ and $n = \nabla \alpha_l$.

The effect of the contact angle between the fluid and the wall is established within the framework of the CSF model (Brackbill et al., 1992) by changing the unit surface normal at the grid next to the wall, which is calculated by the following equation:

$$\tilde{n} = \tilde{n}_w \cos\theta_w + \tilde{m}_w \sin\theta_w \tag{9}$$

where $\tilde{n}_w$ and $\tilde{m}_w$ are the unit vectors normal and tangential to the wall, respectively, and θ_w is the contact angle.

The employment of an appropriate turbulence model is essential for achieving an accurate simulation and different turbulence models have respective adaptability. The two-phase flow in an RPB can be turbulent depending on the packings and the rate of the fluid flow. However, the presence of the packings can have a significant damping effect on the turbulence. The liquid film flow within the boundary layers of the packing surfaces develops from being laminar flow to being fully developed turbulence flow depending the location and thickness of the film and thus can be partially turbulent (Yan et al., 2014), and the Reynolds number based on the size of the pore/wire is usually low. However, in the vicinity of the liquid entrance region and in the cavity region, the Reynolds number is higher. Shi et al. (2013) selected the most elaborate type of turbulence model: the Reynolds stress model (RSM) for the closure of the Reynolds-averaged Navier-Stokes equations. However, in this model, five and seven additional equations should be solved in a 2D and 3D calculation domain, respectively. This substantially increases the calculation time and requires more computational memory. Therefore, several two-equation eddy-viscosity turbulence models, including the standard, shear-stress transport (SST) k-ω models and the standard, RNG, realizable k-ε models with enhanced wall functions, have been tested for seeking the potential to simulate the liquid flow in the RPB. According to the simulation results, when adopting the standard or SST k-ω model, the liquid holdup is within only 5% from that obtained using the RSM model. When adopting the standard k-ε model and its variations, the liquid holdup is always less than when adopting the RSM or k-ω models with an error of about 10%. The SST k-ω model in ANSYS Fluent incorporates modifications for low-Reynolds number effects. Therefore, the SST k-ω model (Menter, 1994) is adopted in this paper. It is worth mentioning that the turbulence modelling in packed materials is currently still a topic of ongoing research.

2.4. Boundary conditions

The computational domain and the locations to which the flow boundary conditions are applied are shown in Fig. 2(b). The liquid inlet is specified by a fixed jet velocity with the volume fraction of the liquid phase being set to unity. The jet velocity ranges from 1.22 m/s to 2.87 m/s, which corresponds to the experimental settings (Yang et al., 2015a). The turbulent intensity is specified as 1%, and the hydraulic diameter is specified as the nozzle width, 1 mm. Many investigations indicate that the gas has little effect on the main liquid flow pattern (Guo et al., 2000) and liquid holdup (Chen et al., 2004; Lin et al., 2000). Therefore, the effect of the gas flow on the liquid flow characteristics is not investigated in this paper. Thus, the volume fraction of the liquid phase and the fluid velocity are set to zero on the rest of the inner boundary. As introduced in Section 2.3, the computational domain is fixed on a rotational coordinate system; therefore, the liquid nozzle rotates in the opposite direction relative to the rotational coordinate system and the movement of the nozzle is realized by a user-defined function (UDF). In the UDF, the position of the liquid nozzle is defined as a function of time and it is updated at each time step during the transient calculation. This nozzle setup method has been verified by comparing the predicted flow patterns and liquid holdup with the sliding mesh method as adopted in the previous research (Shi et al., 2013). The comparison results indicate that the two nozzle setup methods have the same effects while moving the nozzle using the UDF method reduces the complexity of the modelling and presents more flexibility when changing the width of the liquid nozzle without rebuilding the geometry and regenerating the grid.

In the outer periphery of the computational domain, the wall condition is set to simulate the casing wall of the RPB and ten evenly distributed pressure outlets with a depth of 3 mm are set to drain the liquid. The contact angle between the liquid and the wall is set at 150° so as to represent a hydrophobic material, thus the collected liquid can freely move along the wall and quickly drain from the nearest liquid outlet. In addition, there is a gap between the casing wall and the packing region. Therefore, the wall has almost no influence on the flow pattern and the liquid holdup in the packing region, where we pay most of our attention. For the surface of the packing, the no-slip boundary condition and wall adhesion is specified. However, a given packing surface may have different contact angles depending on the liquid properties, and for a given liquid, the contact angle also varies with different packing surfaces (Singh et al., 2016). In addition, the contact angle of the packing surface corresponding to different solvents is not available in the literature. Therefore, in this paper, a value of 30° is specified as the contact angle of the packing surface in the initial simulations. Further, considering the importance of the contact angle on the flow pattern and liquid holdup, the effect of varying the contact angle is investigated in this paper. The computational domain with a rotational speed of the reference frame in the range of 500–1500 rpm is used to investigate the effect of the rotational speed of the PRB on the flow.

2.5. Solvent properties

Aqueous monoethanolamine (MEA) solution is one of the typical absorbents for CO_2 capture. Previous investigations showed that increasing the concentration of the MEA solution can greatly increase the CO_2 absorption capacity (Jassim et al., 2007) and reduce the absorbent's regeneration energy (Abu-Zahra et al., 2007). The RPB has the advantage to cope with a highly concentrated MEA solution than packed columns because of the strong centrifugal field (Chen et al., 2005) that can significantly increase the specific surface area of the solvent, but the effect of the liquid concentration on the liquid flow characteristics in RPBs has never been investigated through CFD modelling. Therefore, simulations are performed with a variety of aqueous MEA solutions. In addition, for the model validation, water and glycerol are also adopted. The properties of the solvents used for the CFD simulations are shown in Table 1. The MEA is assumed to operate at a constant temperature of 40 °C, which is close to the real operation conditions of a CO_2 absorber employed for PCC.

2.6. Solution procedure

Transient simulations are performed using the ANSYS Fluent 16.1 code that incorporates the in-house developed UDF in a double precision mode. The pressure-velocity coupling is resolved by the PISO algorithm, and the PRESTO scheme is employed for the pressure discretization. The Geo-Reconstruct method is applied for the spatial discretization of the volume fraction equation, the second-order upwind scheme is employed for solving the momentum equations and turbulence equations. In addition, for the convergence criteria, the residuals of the mass balance equations are taken to be less than 1×10^{-4} and the residuals of all the other equations are less than 1×10^{-5}. Different time step sizes have been tested to check the effect of the time step size on the results. As a result, the time step size is set as 1×10^{-5} s when the rotational speed is between 500 and 750 rpm (include 750 rpm) and 5×10^{-6} s when the rotational speed is between 750 and 1500 rpm. In addition, the maximum number of iterations of 30 are performed per time step in order to achieve the calculation convergence. The instantaneous liquid holdup is monitored for each simulation to make sure it achieves the pseudo steady state and the average liquid holdup in each simulation is calculated based on the instantaneous liquid holdup after the simulation achieving the pseudo steady state.

2.7. Grid independence

A grid independence study is conducted to determine a reasonable computational grid. Four different grids consisting of 0.13, 0.43, 0.64 and 0.87 million quadrilateral-dominated cells have been employed to investigate the effect of the mesh on the CFD solutions. The grid is refined at the vicinity of the packing surface. When increasing the grid numbers in the packing surface, the

Table 1
Physical properties of the solvents used for the CFD simulations.[a]

Solvent	Density/(kg/m^3)	Viscosity/(Pa·s)	Surface tension/(N/m)
Water	998.2	0.001003	0.0728
30 wt% MEA (Amundsen et al., 2009)	1003.4	0.00167	0.05352
50 wt% MEA (Amundsen et al., 2009)	1011.7	0.00339	0.05069
70 wt% MEA (Amundsen et al., 2009)	1015.5	0.00696	0.04888
90 wt% MEA (Amundsen et al., 2009)	1008.4	0.0102	0.04725
60 wt% glycerol (Yang et al., 2015a)	1140	0.00938	0.0669
70 wt% glycerol (Yang et al., 2015a)	1172.95	0.0185	0.0665
80 wt% glycerol (Yang et al., 2015a)	1213.6	0.0558	0.0657

[a] The properties of the aqueous MEA solutions are at 40 °C.

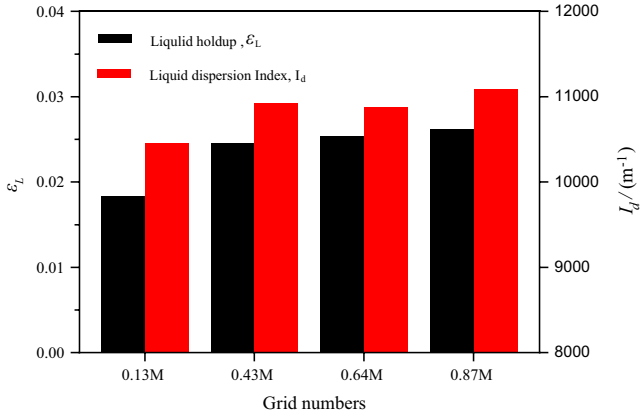

Fig. 4. Predicted liquid holdup and liquid dispersion index using four different grids. (N = 1500 rpm, u_0 = 1.53 m/s, water).

regions, which are away from the packing surface, can correspondingly be refined according to the meshing strategy employed. As shown in Fig. 4, solutions for the liquid holdup and the liquid dispersion index (explained in Section 3.4.1) at a demanding condition are almost the same as when using a grid with no less than 0.43 M cells, which may be regarded as a reasonable fine grid to predict the overall liquid flow characteristics. Therefore, for the simulations of the liquid holdup and the liquid dispersion index, the grid with 0.43 M cells is used as a trade-off between computing time and simulation precision. However, a refined grid can achieve a clearer observation of the detailed liquid flow pattern. Therefore, for investigating the liquid flow pattern, the 0.87 M grid is chosen.

3. Results and discussion

3.1. Model validation

The CFD predicted liquid holdup has been compared with the experimental results measured by Yang et al. (2015a) and with the correlation proposed by Burns et al. (2000) as follows:

$$\varepsilon_L = 0.039\left(\frac{g}{g_0}\right)^{-0.5}\left(\frac{U}{U_0}\right)^{0.6}\left(\frac{\nu}{\nu_0}\right)^{0.22} \quad (10)$$

where $g_0 = 100\ \mathrm{m/s^2}$, $U_0 = 0.01\ \mathrm{m/s}$ and $\nu_0 = 10^{-6}\ \mathrm{m^2/s}$ are characteristic values.

This correlation has been adopted by many researchers for validation (Yang et al., 2016) and process modelling (Joel et al., 2015, 2014; Kang et al., 2014, 2016) of RPBs. The simulation results in this paper show that the effect of the rotational speed (Fig. 5(a)), the liquid jet velocity (Fig. 5(b)) and the liquid viscosity (Fig. 5(c)) on the liquid holdup is similar to those obtained by Yang et al. (2015a) experimentally and the Burns correlation. It is noted that the liquid holdup from the simulation is closer to the experiments than the widely accepted Burns correlation. This may be because the conductivity measurement method adopted in the experiments (Burns et al., 2000) cannot take into consideration of the free droplets, which take up an important percentage of liquid in the packing region of typical RPBs. However, the liquid holdup from the simulation is still lower than the liquid holdup obtained by the X-ray technique in general. On the one hand, this is because the liquid may accumulate at the intersections of the two crossed wires but this cannot be considerate in this 2D model. On the other hand, because the concentric wires are ignored in the 2D model, the specific area (469 m^{-1}) of the packing in the model is slightly less than that of the real packing (497 m^{-1}) although the void fraction of the packing (0.94) in the 2D model is similar to that in the

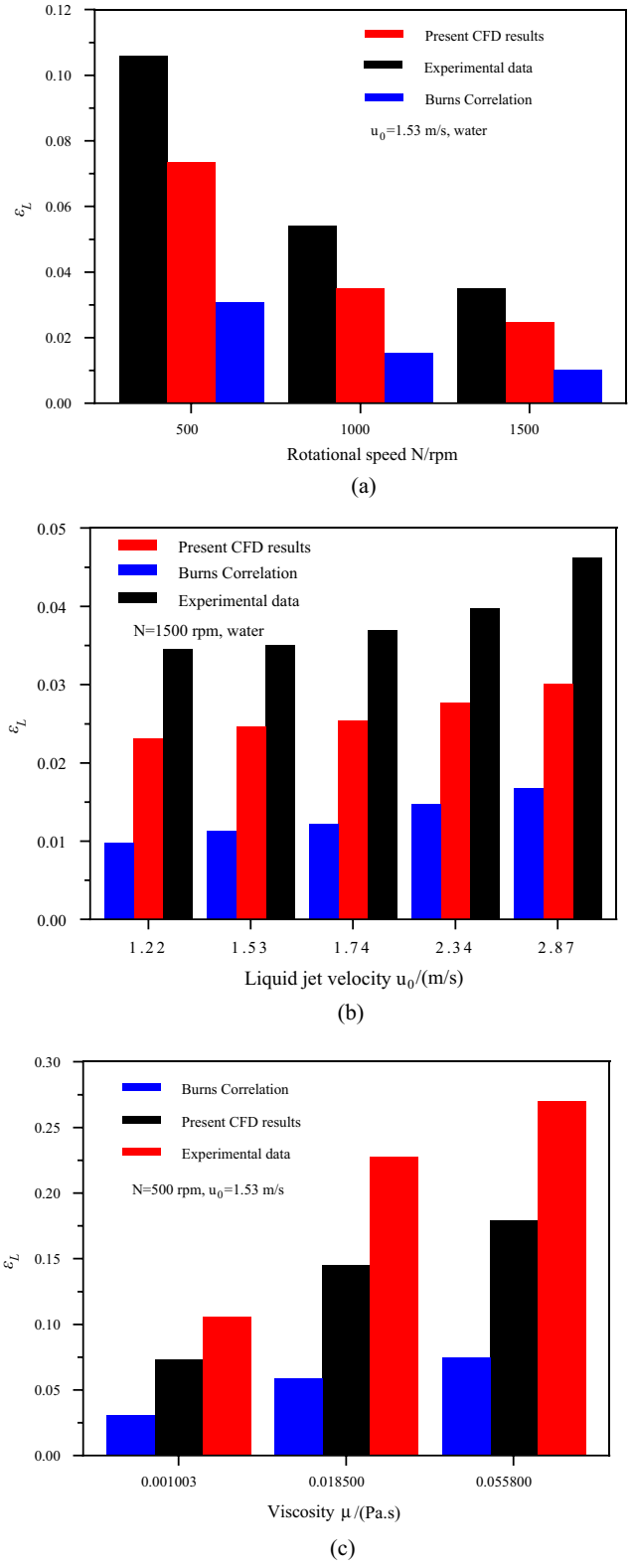

Fig. 5. Comparison of simulation results of liquid holdup with the experimental data (Yang et al., 2015a) and Burns correlation (Burns et al., 2000): (a) Effect of the rotational speed, (b) effect of the liquid jet velocity, and (c) effect of the liquid viscosity.

experiments (0.95). Therefore, there is less packing surface to be wetted by the liquid. In general, this model can reflect the effects of the above-mentioned influencing factors on the liquid holdup, compared to the experimental data obtained by Yang et al.

(2015a). Although the simulation is performed in a 2D domain rather than a real 3D domain and there are some limitations due to the simplification of the real geometry, we take the view that the 2D CFD model can still effectively predict the liquid flow characteristics in the RPB. Nevertheless, with the increase in the computer power in the future, performing full 3D simulation of the RPB can obtain more detailed and more accurate results.

3.2. Liquid flow pattern in the RPB

Solvents with 30 wt% MEA are typically recommended to be used in conventional packed bed absorbers. However, the RPB can cope with much higher MEA concentrations. In this paper, the 50 wt% aqueous MEA solution is used to demonstrate the liquid flow patterns in the RPB. The CFD model predicted four typical liquid flow patterns in two different packing regions and under two rotational speeds of the RPB are shown in Fig. 6. As can be seen in Fig. 6, or Fig. 2(b), the packing space is unevenly distributed in the whole packing region. The arrangement of the wires in the CFD model is similar to the inherent nature of the random wire mesh packing, since the wire mesh is compactly arranged in rolls, which forms regular but an uneven distribution around the bed. The distribution of the wires in different circumferential regions of the packing has more or less effect on the liquid flow pattern, however distinct flow patterns still can be observed in different packing regions around the bed, which are mainly determined by the radial positions and the operation conditions. The packing region close to the liquid inlet is usually defined as the entrance region, which is the region of about 10 mm in radius in the inner side of the dashed lines as indicated in Fig. 6. The rest of the packing region is usually defined as the bulk region. Also, different flow patterns between the two regions have been confirmed by Guo et al. (2000), Yan et al. (2012) and Guo et al. (2014) through different experimental methods, which indicate the feasibility of the CFD model to investigate the liquid flow pattern in the RPB.

3.2.1. Flow pattern in the entrance region

As shown in Fig. 6, when the liquid is injected into the packing region from the liquid inlet, the rotational packing splits the liquid continuously. Most of the liquid is sheared into the liquid ligaments but still moves almost along the radial direction, which is mainly due to the existence of the initial momentum in the radial direction. A small percentage of the liquid becomes liquid films and it adheres to the packing wires and rotates with the packing. As for the liquid ligaments in the entrance region, the radial velocity of the liquid decreases from the initial jet velocity to a lower velocity. This is mainly due to the loss of the liquid initial momentum when the liquid strikes the packing. However, the tangential velocity of the liquid gradually increases from zero to approach the packing's tangential velocity under the action of the drag force from the packing. As a result, the ratio of the tangential velocity to the radial velocity of the liquid ligaments gradually increases, and the liquid ligaments are all captured by the packing at the end of the entrance region.

3.2.2. Flow pattern in the bulk region

Within the bulk region, at a relatively low rotational speed, such as 500 rpm, where the average centrifugal acceleration in the bed

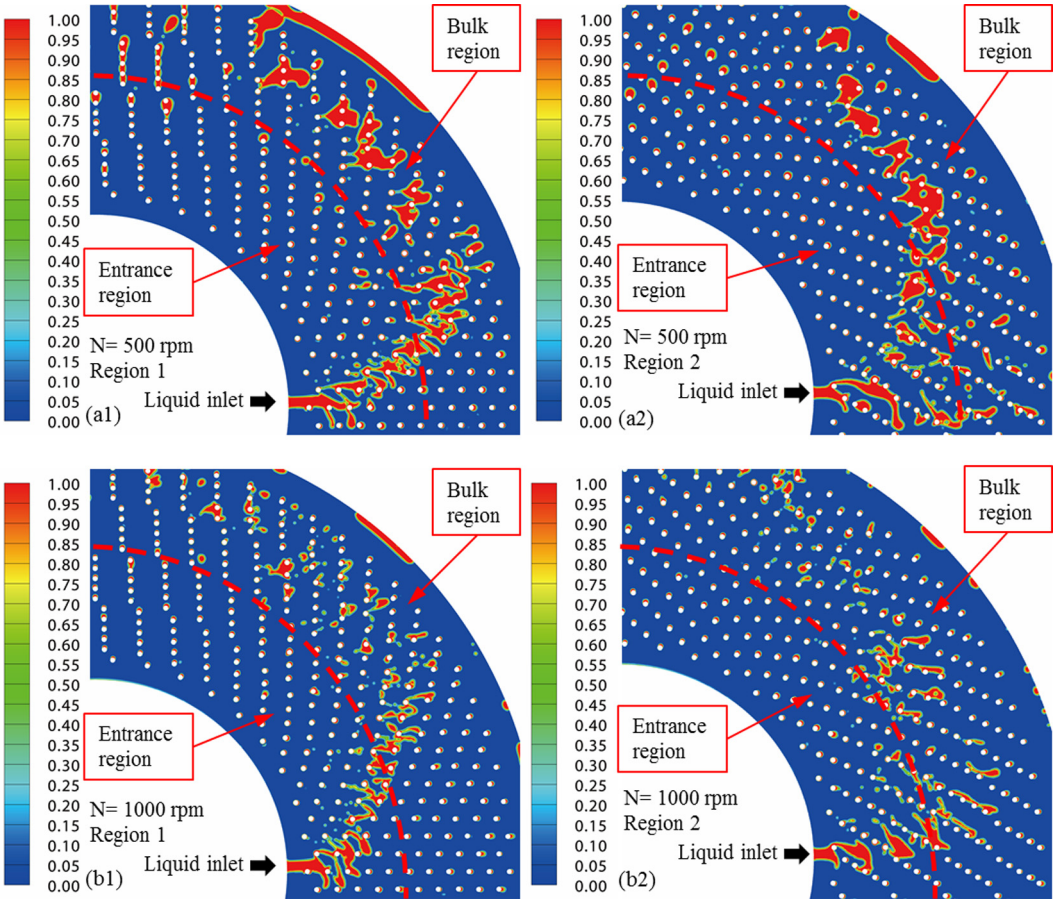

Fig. 6. Typical liquid flow patterns in different regions (50 wt% MEA, u_0 = 2.87 m/s).

is about 80 m/s^2, the liquid flow pattern is a pore-dominated flow, as shown in Fig. 6(a1) and (a2). This is because the surface tension makes the liquid prefer to coalesce and the relative velocity between the liquid and the packing is not large enough to make it separate. As a result, the liquid exists in the form of liquid groups and travels in the pores of the packing. While at a higher rotational speed, such as 1000 rpm, where the average centrifugal acceleration in the bed is about 320 m/s^2, the liquid flow pattern becomes a droplet-dominated flow, as shown in Fig. 6(b1) and (b2).

The typical transportation process of a droplet in the bulk region of the packing is shown in Fig. 7. It shows that the liquid moves relative to the rotating packing at 1000 rpm within seven milliseconds. Initially, the observation is focused on the droplet within the dashed circles in Fig. 7(a) at time t_0. Then the droplet moves, disperses and mixes with other liquid as time goes on. The liquid elements, which originated from the same droplet within the red dashed circle in Fig. 7(a), are marked by the dashed circles in the rest of the figures. As can be observed, when the liquid droplet hits the packing surface and one part of the liquid attaches to the packing surface and becomes a liquid film, and the other part of the liquid moves into the next layer of the packing space. The percentage of the free moving liquid relative to the captured liquid by the packing surface depends on the voidage of the packing, that is, a higher voidage leads to a higher percentage of free moving liquid to the next layer. As for the captured liquid by the packing surface, when the liquid leaves the surface of the wires, the stretched liquid droplets always breakup and generate some satellite droplets (see Fig. 7(d) and (h)). This is because the surface tension of the liquid makes it have the trend to form liquid droplets rather than liquid ligaments. At the same time, the droplet–droplet collisions occur in the packing space, see Fig. 7(e)–(f), and the small droplets collide and merge into big droplets. These steps repeat until the liquid moves out of the packing region and the droplets become smaller and smaller and the liquid surfaces continuously update.

3.3. Liquid holdup and liquid residence time in the RPB

The liquid holdup (ε_L), defined as the liquid volume per unit packing volume, and the mean residence time ($\bar{t}$) of the liquid are two essential parameters for an RPB (Burns et al., 2000; Guo et al., 2000; Yang et al., 2015a) and the two parameters are closely related. The mean residence time of liquid can be determined based on the liquid holdup using the following equation (Burns et al., 2000):

$$\bar{t} \approx \frac{\varepsilon_L}{U}(r_0 - r_1) \tag{11}$$

where r_0 and r_1 are radial positions of the outer and inner packing and U is the superficial liquid flow velocity and can be calculated by

$$U = \frac{u_0 d}{2\pi r} \tag{12}$$

where u_0 is the liquid jet velocity, d is the width of the nozzle and $r = (r_0 + r_1)/2$.

3.3.1. Effect of rotational speed on liquid holdup

Fig. 8 shows the effect of the rotational speed (ω) on the liquid holdup at two different liquid jet velocities where the 50 wt% aqueous MEA solution is used. The figure illustrates that the liquid holdup decreases with the increasing rotational speed from 500 to 1500 rpm for both liquid jet velocities of 1.53 and 2.87 m/s. The liquid gains the tangential velocity from the packing continuously, and it almost synchronously rotates with the packing in the bulk region. Therefore when increasing the rotational speed, the liquid can obtain a higher tangential velocity, thus resulting in a higher centrifugal acceleration as well as a higher radial velocity relative to the packing. Therefore, the residence time of the liquid decreases as well as the liquid holdup decreases.

In addition, on increasing the rotational speed, the liquid can gain more kinetic energy from the packing, and the liquid can be split into smaller liquid droplets and fragments (compare Fig. 6(a1) and (b1) or compare Fig. 6(a2) and (b2)). Therefore, the percentage of liquid that flies into the void of the packing free from the drag force from the packing increases, which also contributes to the increasing average radial velocity. As shown in Fig. 8, on increasing the rotational speed from 500 to 1000 rpm, where the liquid flow is dominated by the pore flow, the liquid holdup decreases by about 50%. While, when increasing the rotational speed from 1000 rpm to 1500 rpm, the liquid holdup decreases by only about 20% and this may be because the droplets are difficult to be captured by the packing when the rotational speed is higher than 1000 rpm, where the liquid flow is dominated by the droplet flow and the droplets become smaller and smaller.

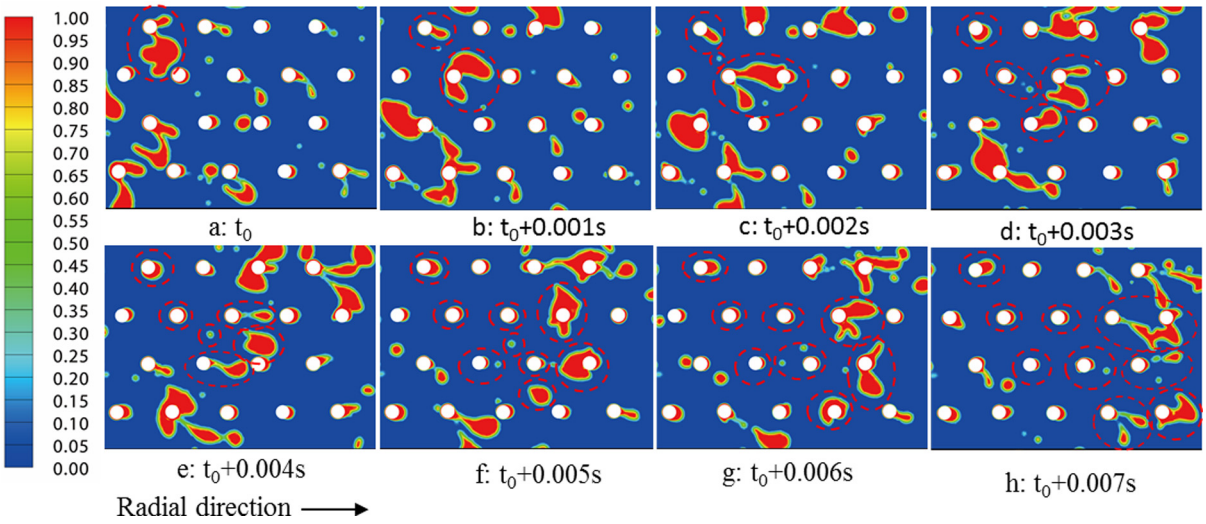

Fig. 7. Transient development of the liquid phase (50 wt% MEA, N = 1000 rpm, u_0 = 1.53 m/s).

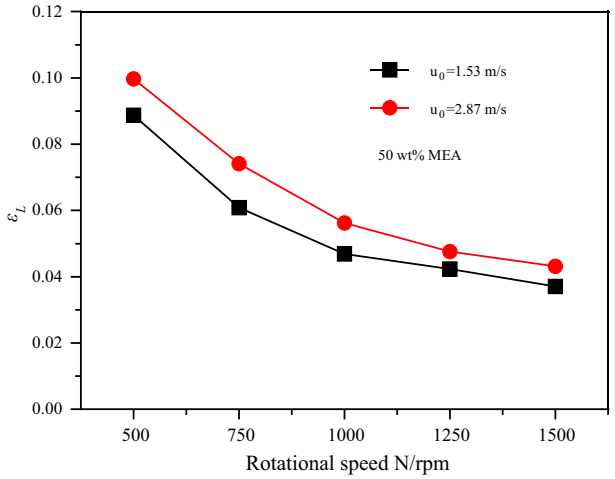

Fig. 8. Effect of the rotational speed on the liquid holdup.

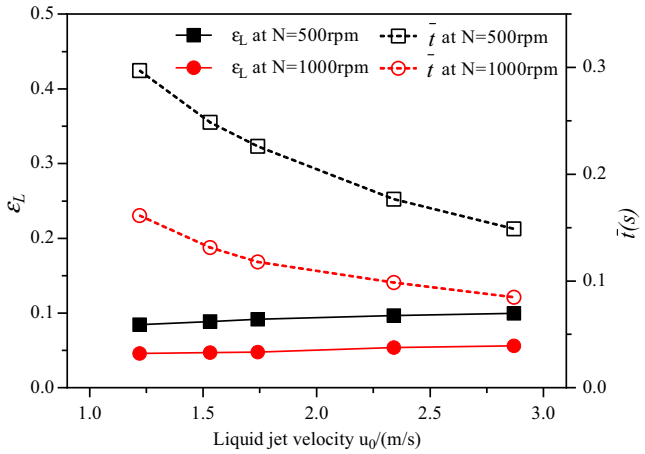

Fig. 9. Effect of the liquid jet velocity on the liquid holdup and the residence time.

From Fig. 7(e) to (h), it can be observed that some of the liquid is retained in the packing surface and does not move with time, and this is due to the adhesion force between the liquid and the packing surface. In this state, the centrifugal force and the adhesion force are in balance. When the rotational speed increases, then the retained liquid obtains a higher centrifugal force, and when the adhesion force cannot meet the centrifugal force, then the retained liquid moves away from the packing surface. Therefore, the percentage of the retained liquid decreases with increasing rotational speed, which also leads to the decrease in the liquid holdup.

3.3.2. Effect of liquid jet velocity on liquid holdup and residence time

The effect of the liquid jet velocity on the liquid holdup is shown in Fig. 9. It is clear that the liquid holdup increases with the increasing liquid jet velocity, while, the increase rate of the liquid holdup is very small. This is because the average liquid radial velocity increases with increasing the liquid jet velocity. Specifically, a higher liquid jet velocity directly increases the liquid radial velocity in the entrance region. In addition, with an increase in the liquid flow rate, the frequency of the liquid-liquid collisions and liquid-packing collisions increases, therefore small droplets and thin films are easier to coalescence and form big droplets, which increases the escape frequency of the liquid from the packing surface. Due to the same reason, the liquid residence time decreases with the increasing liquid jet velocity, as shown in Fig. 9. As for the flow pattern, on comparing Fig. 10(a) and (b), with an increase in the liquid jet velocity, the radial distance of the entrance region increases and the circumferential liquid maldistribution is more severe.

3.3.3. Effect of MEA concentration on liquid holdup and liquid residence time

The effect of the MEA concentration on the liquid holdup is shown in Fig. 11, which shows that the liquid holdup increases with the increasing MEA concentration from 30 wt% to 90 wt%. This is mainly because the liquid viscosity noticeably increases with the increasing concentration of the MEA. As shown in Fig. 12, most of the liquid is partially in contact with the packing surface where the viscous force plays a major role. With the increasing of the liquid viscosity, the liquid deformation rate reduces and this causes the residence time of the liquid that is partially attached onto the packing surface to increase. In addition, the thickness of the boundary layer increases with the increasing liquid viscosity and this leads to the liquid volume that is attached to the packing surface to increase. Thus, the liquid holdup increases with an increasing liquid viscosity. From another perspective, the drag force is the driving force for the liquid movement in the tangential direction, but it is resistant to the liquid movement in the radial direction. As a result, with increasing the liquid viscosity, the liquid is easier to attach onto the packing surface and follow the rotation of the packing, which leads to a better circumferential liquid distribution (compare Fig. 12(a) and Fig. 12(b) or

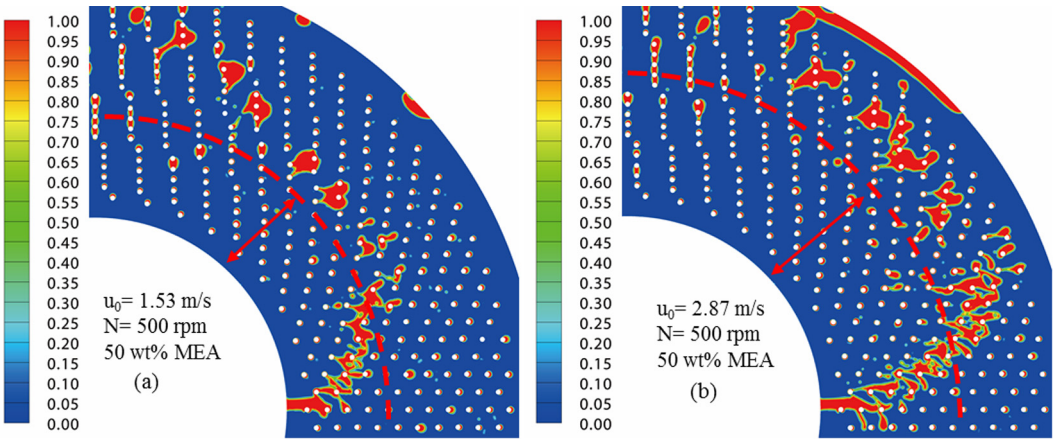

Fig. 10. Effect of the liquid jet velocity on the liquid flow pattern.

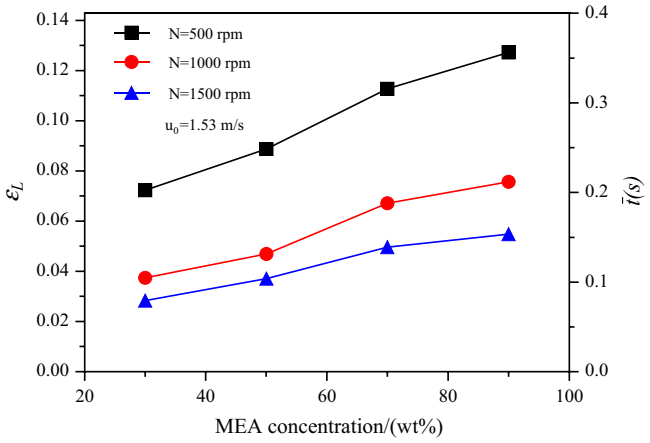

Fig. 11. Effect of the MEA concentration on the liquid holdup and the liquid mean residence time at two different rotational speeds.

compare Fig. 12(c) and (d)). Also, this contributes to the increasing of the liquid holdup.

However, as shown in Fig. 11, the effect of the MEA concentration on the liquid holdup is weaker at a higher rotational speed. This is because at a higher rotational speed, the free moving liquid droplets increases and the amount of the liquid films attached to the packing surface reduces and thus the influence of the viscous resistance force on the liquid becomes weaker. Such as, at 500 rpm, the flow pattern is pore-dominated flow, and much liquid is in contact with the packing surface, thus the liquid viscosity has a stronger influence on the liquid holdup than that at 1000 rpm or 1500 rpm, where the liquid is in the droplet-dominated flow pattern.

When keeping the liquid jet velocity as constant, the mean residence time of the liquid ($\bar{t}$) is proportional to the liquid holdup based on Eq. (12). Therefore, the effect of the MEA concentration on $\bar{t}$ is the same as the effect of the MEA concentration on the liquid holdup and the value of $\bar{t}$ can be obtained from the right Y-axis of Fig. 11.

3.3.4. Effect of contact angle on liquid holdup and liquid residence time

The contact angle is an important parameter for gas-liquid-solid systems and different packing materials and/or different surface treatments lead to different contact angles. Stainless steel is hydrophilic but some materials used in the RPB packing are hydrophobic (Zheng et al., 2016). In order to cover a wide range of materials, the effect of the contact angles from 0 deg, where complete wetting occurs (Yuan and Lee, 2013), to 150 deg on the liquid holdup and flow pattern is investigated. The increasing of the contact angle means the wettability of the packing by the liquid is not as good. Fig. 13 shows that the liquid holdup is reduced with the increasing of the contact angle. When the contact angle is less than 90 deg, the material is hydrophilic (see Fig. 14(a)). At a certain rotational speed, with an increase in the contact angle, the percentage of the liquid that is attached to the packing surface decreases. Moreover, on increasing the contact angle, the flow pattern transformation, i.e. from the pore-dominated flow to the droplet-dominated flow, occurs at a lower rotational speed. When the contact angle is larger than 90 deg, the material is hydrophobic (see Fig. 14(b)). Therefore, when the liquid-packing collision occurs, the liquid is almost impossible to be attached on to the packing surface. Further, with the increasing of the contact angle, more small droplets are generated. This phenomenon also has been observed in the experimental work of Zheng et al. (2016). Because the packing

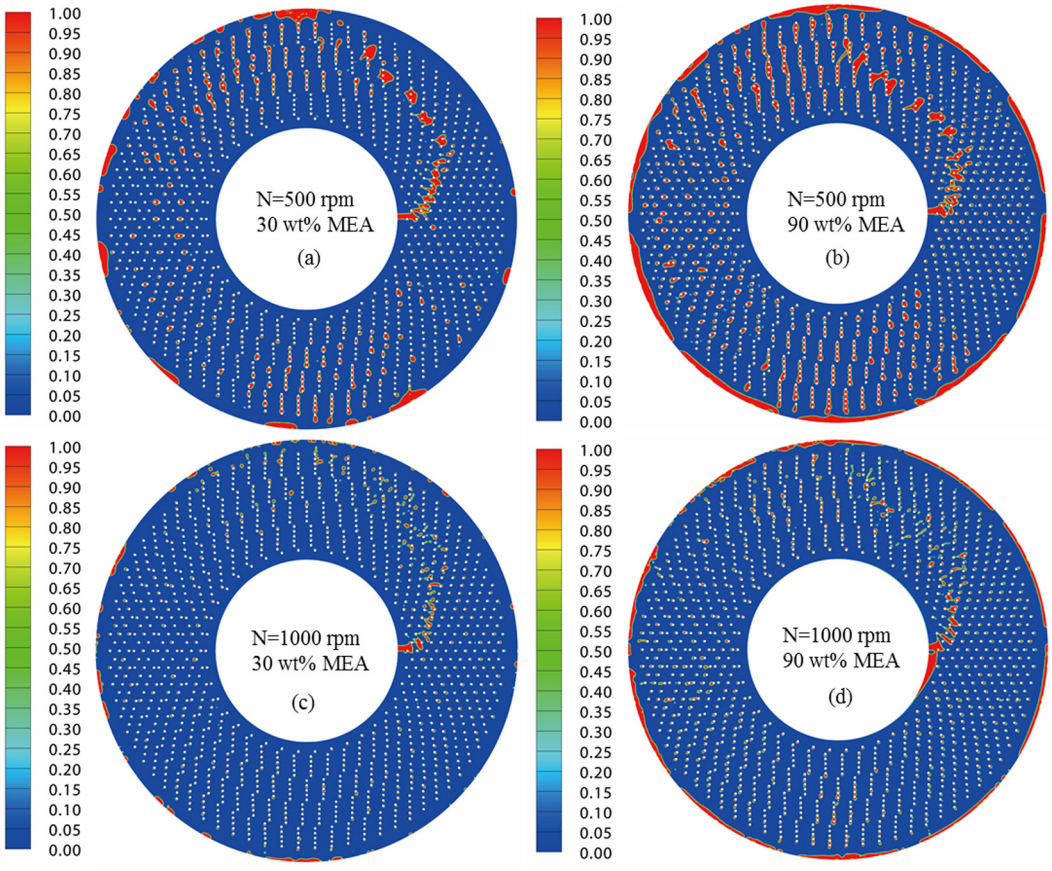

Fig. 12. Effect of MEA concentration on the liquid flow pattern at different rotational speeds (u_0 = 1.53 m/s).

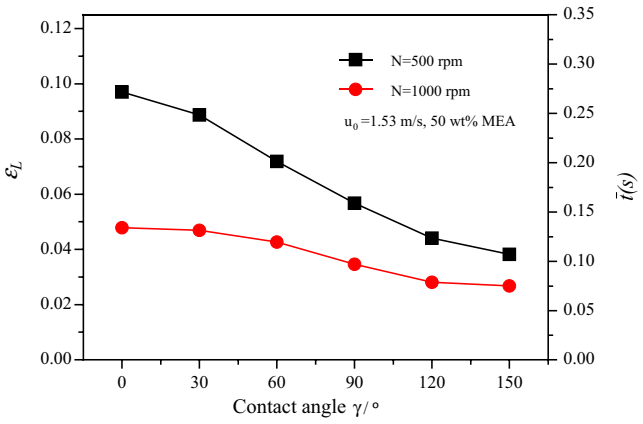

Fig. 13. Effect of the contact angle on the liquid holdup and the liquid mean residence time at two different rotational speeds.

has no viscous resistance on the flying liquid droplets, a large percentage of liquid droplets means a higher average radial velocity and this decreases the liquid holdup. The value of $\bar{t}$ is marked on the right Y-axis of Fig. 13.

3.4. Liquid dispersion

3.4.1. Definition of the liquid dispersion index (I_d)

The reaction between CO_2 and MEA is fast and the absorption of CO_2 is usually mass transfer limited (Jassim et al., 2007), and therefore the enhancement of the CO_2 absorption in an RPB mainly depends on the liquid dispersion to increase the interfacial area. Highly dispersed liquid can generate a large gas-liquid interface and increase the surface renewal rate of the liquid due to the higher turbulence. The degree of liquid dispersion is usually assessed based on the droplet size and film thickness. However, due to the complex packing structure and the high frequent interactions between the liquid and the packing surface, different liquid shapes, such as liquid droplets, liquid films, liquid ligaments and liquid groups, co-exist in the packing region. Therefore, it is extremely difficult to assess the overall degree of liquid dispersion based on the common parameters such as droplet size and/or film thickness. In this paper, a liquid dispersion index (I_d) is defined as follows in order to assess the degree of liquid dispersion:

$$I_d = \frac{A_{int}}{V_l} \tag{13}$$

where A_{int} is the gas-liquid interfacial area in the packing region, and V_l is the liquid volume in the packing region. In the VOF model, the liquid volume fraction (α_l) of 0.5 is used to define the gas-liquid interface (Lan et al., 2010). The liquid dispersion index (I_d) is similar to the specific surface area of the liquid in the packing region of the RPB but it only considers the gas-liquid interfacial area, which is effective for the gas-liquid mass transfer. The liquid-solid interfacial area is not considered in this parameter.

3.4.2. Effect of MEA concentration and rotational speed on I_d

As shown in Fig. 15, the liquid dispersion index (I_d) decreases with the increasing of the MEA concentration from 30 wt% to

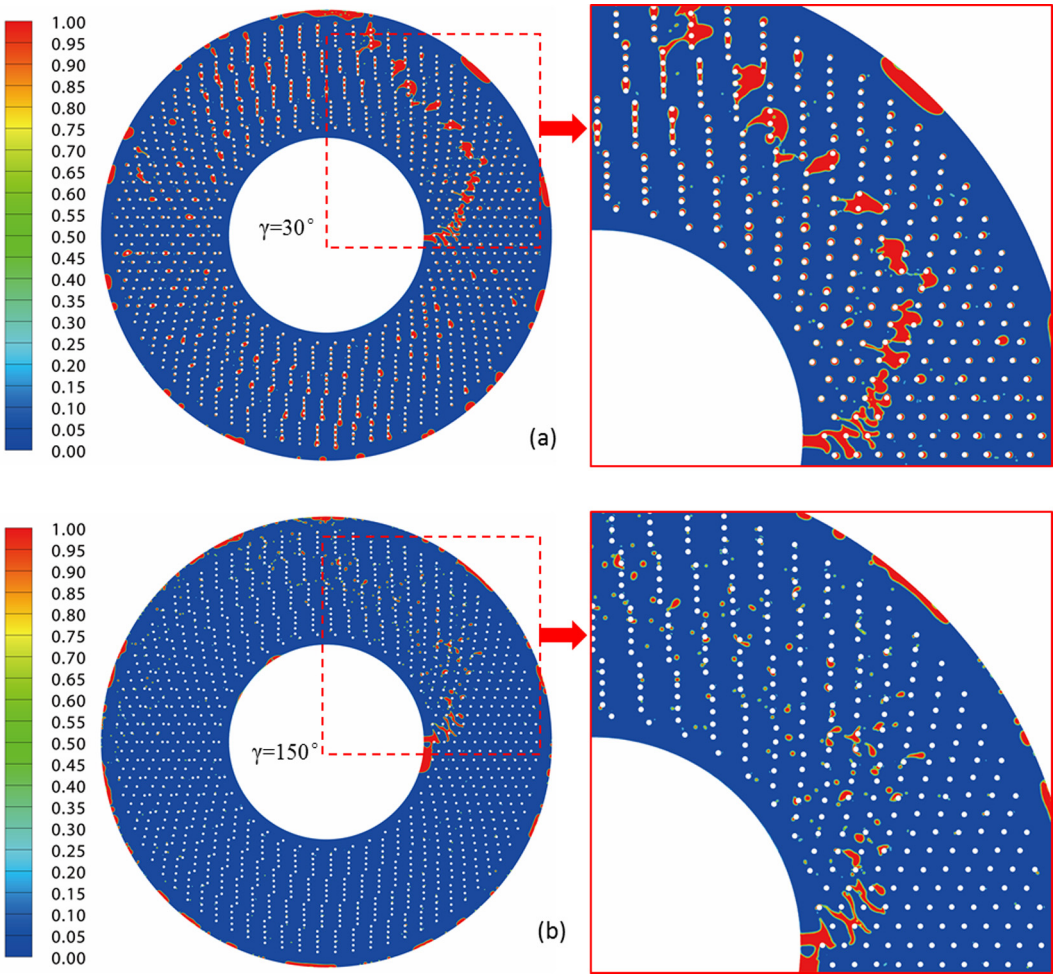

Fig. 14. Effect of the contact angle on the liquid flow pattern (50% MEA, N = 500 rpm, u_0 = 1.53 m/s).

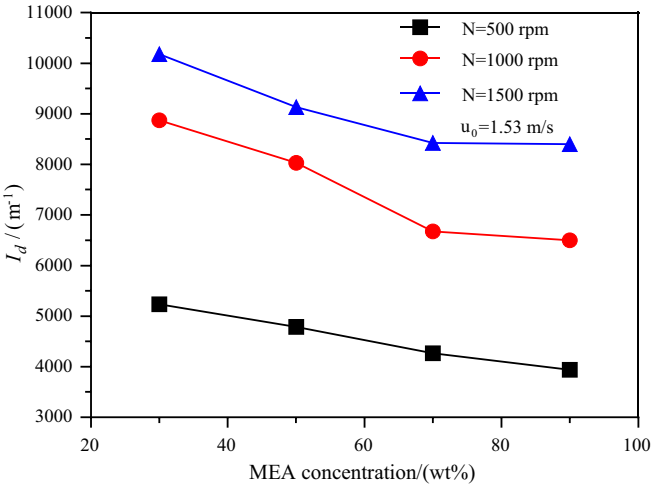

Fig. 15. Effect of the MEA concentration on the liquid dispersion index at three different rotational speeds.

90 wt%. This is because, with the increasing of the liquid viscosity, the film thickness increases and the size of other discrete liquid, such as the liquid droplets and the liquid ligaments, may increase as well because the discrete liquid particles are mainly derived from the separation of liquid films from the packing surface. Meanwhile, at a constant rotational speed, the relative velocity between the liquid and the packing is smaller at a higher MEA concentration due to the effect of viscous damping. Therefore, the liquid breakup is more difficult to occur. In addition, it demonstrates that with the increasing of the rotational speed, I_d is remarkably increased, especially from 500 rpm to 1000 rpm, where the flow pattern transforms from being a pore-dominated flow to a droplet-dominated flow (Comparing Fig. 12(a) and Fig. 12(c) or Fig. 12(b) and Fig. 12(d)).

3.4.3. Effect of contact angle on I_d

The effect of the contact angle on the liquid dispersion index (I_d) at 500 rpm and 1000 rpm is shown in Fig. 16, where it can be seen that when the contact angle is less than 90 deg, that is, when the packing material is hydrophilic, I_d markedly decreases with the increasing of the contact angle. This is because the liquid is less likely to cover the packing surface and stretches into thin films

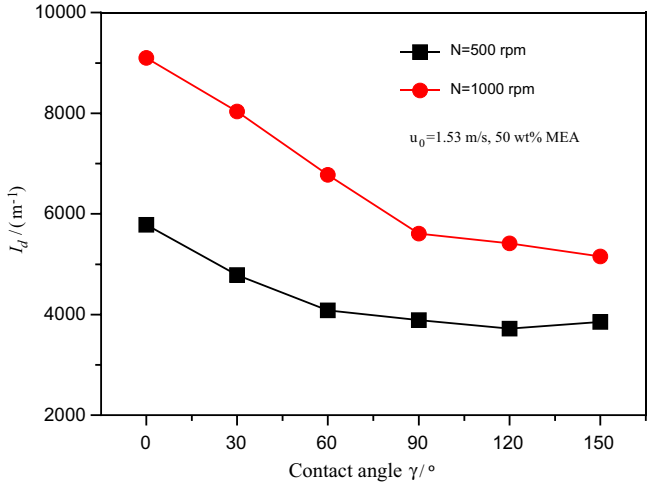

Fig. 16. Effect of the contact angle on the liquid dispersion index at two different rotational speeds.

at a higher contact angle. When the contact angle is larger than 90 deg, that is, as for the hydrophobicity packing material, the contact angle has less effect on the I_d compared to the hydrophilic materials and this may be due to the liquid mainly existing in the droplet form and almost no liquid film covers the packing surface. However, with the increasing of the contact angle, a larger percentage of small droplets are generated and this phenomenon is more dominated at lower rotational speeds. Therefore, the increased surface area due to the increasing percentage of small droplets compensates the decreased surface area due to less liquid film being formed. Therefore, the decreasing rate of I_d with increasing contact angle under a lower rotational speed is lower than under a higher rotational speed.

4. Conclusions

A 2D CFD model has been built to investigate the liquid behaviour in an RPB. The model has been verified through comparing the results obtained with the available experimental data (Yang et al., 2015a) and the Burns correlation (Burns et al., 2000). The results show that the 2D CFD model is effective in analysing the liquid flow characteristics in the RPB. Both the overall and local liquid flow patterns in the RPB have been analysed and distinct flow patterns have been observed in different packing regions. In the entrance region, the liquid flow is ligament-dominated flow; in the bulk region, the flow pattern is pore-dominated flow at low rotational speeds (500–1000 rpm) and droplet-dominated flow at high rotational speeds (1000–1500 rpm). The results show that the size of the entrance region increases with increasing the liquid jet velocity. With the increasing rotational speed, whilst the degree of liquid dispersion increases, the liquid holdup and residence time decrease. This is because more liquid is in droplet form and there is a thinner film flow. However, under the simulation conditions, the liquid holdup slightly increases with the increasing liquid jet velocity. When a high concentration MEA is employed, the liquid dispersion decreases but the liquid holdup and residence time increases and the effect is weak at a relatively high rotational speed. The liquid holdup and flow pattern are sensitive to the contact angle. Larger contact angles can generate more liquid droplets while smaller contact angles can generate more liquid films. The simulation results indicate that this CFD modelling method has the capability of analysing the detailed liquid flow patterns, the liquid holdup, the liquid residence time as well as the degree of liquid dispersion in an RPB. Because of the acceptable computational accuracy and much smaller amount of computations compared to a 3D model, this method has the potential to be used to analyse the hydrodynamics of an industrial scale RPB.

Acknowledgment

P. Xie would like to acknowledge the China Scholarship Council and the University of Sheffield for funding his research studies. The authors also acknowledge the support from the EPSRC grant (EP/M001458/2, Process Intensification for Post-combustion Carbon Capture using Rotating Packed Bed through Systems Engineering Techniques).

References

Abu-Zahra, M.R.M., Schneiders, L.H.J., Niederer, J.P.M., Feron, P.H.M., Versteeg, G.F., 2007. CO2 capture from power plants. Part I. A parametric study of the technical-performance based on monoethanolamine. Int. J. Greenhouse Gas Control 1, 37–46. http://dx.doi.org/10.1016/S1750-5836(06)00007-7.

Amundsen, T.G., Oi, L.E., Eimer, D.A., 2009. Density and viscosity of monoethanolamine plus water plus carbon dioxide from (25 to 80) °C. J. Chem. Eng. Data 54, 3096–3100. http://dx.doi.org/10.1021/je900188m.

ANSYS Inc, 2015. Theory Guide of ANSYS Fluent 16.1.
Basic, A., Dudukovic, M.P., 1995. Liquid holdup in rotating packed-beds – examination of the film flow assumption. AIChE J. 41, 301–316. http://dx.doi.org/10.1002/aic.690410212.
Brackbill, J.U., Kothe, D.B., Zemach, C., 1992. A continuum method for modeling surface-tension. J. Comput. Phys. 100, 335–354. http://dx.doi.org/10.1016/0021-9991(92)90240-Y.
Burns, J.R., Jamil, J.N., Ramshaw, C., 2000. Process intensification: operating characteristics of rotating packed beds – determination of liquid hold-up for a high-voidage structured packing. Chem. Eng. Sci. 55, 2401–2415. http://dx.doi.org/10.1016/s0009-2509(99)00520-5.
Burns, J.R., Ramshaw, C., 1996. Process intensification: visual study of liquid maldistribution in rotating packed beds. Chem. Eng. Sci. 51, 1347–1352. http://dx.doi.org/10.1016/0009-2509(95)00367-3.
Chen, J.F., Gao, H., Zou, H.K., Chu, G.W., Zhang, L., Shao, L., Xiang, Y., Wu, Y.X., 2010. Cationic polymerization in rotating packed bed reactor: experimental and modeling. AIChE J. 56, 1053–1062. http://dx.doi.org/10.1002/aic.11911.
Chen, J.F., Wang, Y.H., Guo, F., Wang, X.M., Zheng, C., 2000. Synthesis of nanoparticles with novel technology: high-gravity reactive precipitation. Ind. Eng. Chem. Res. 39, 948–954. http://dx.doi.org/10.1021/ie990549a.
Chen, Y.H., Chang, C.Y., Su, W.L., Chen, C.C., Chiu, C.Y., Yu, Y.H., Chiang, P.C., Chiang, S.I.M., 2004. Modeling ozone contacting process in a rotating packed bed. Ind. Eng. Chem. Res. 43, 228–236. http://dx.doi.org/10.1021/ie030545c.
Chen, Y.S., Lin, C.C., Liu, H.S., 2005. Mass transfer in a rotating packed bed with viscous newtonian and non-Newtonian fluids. Ind. Eng. Chem. Res. 44, 1043–1051. http://dx.doi.org/10.1021/ie0499409.
Chen, Y.S., Lin, F.Y., Lin, C.C., Tai, C.Y.D., Liu, H.S., 2006. Packing characteristics for mass transfer in a rotating packed bed. Ind. Eng. Chem. Res. 45, 6846–6853. http://dx.doi.org/10.1021/ie060399l.
Chen, Y.S., Liu, H.S., 2002. Absorption of VOCs in a rotating packed bed. Ind. Eng. Chem. Res. 41, 1583–1588. http://dx.doi.org/10.1021/ie010752h.
Cheng, H.H., Lai, C.C., Tan, C.S., 2013. Thermal regeneration of alkanolamine solutions in a rotating packed bed. Int. J. Greenhouse Gas Control 16, 206–216. http://dx.doi.org/10.1016/j.ijggc.2013.03.022.
Chu, G.W., Luo, Y., Shan, C.Y., Zou, H.K., Xiang, Y., Shao, L., Chen, J.F., 2014. Absorption of SO_2 with ammonia-based solution in a cocurrent rotating packed bed. Ind. Eng. Chem. Res. 53, 15731–15737. http://dx.doi.org/10.1021/ie502519v.
Gao, Z.M., Ma, S.G., Shi, D.T., Wang, J.N., Bao, Y.Y., Cai, Z.Q., 2015. Droplet characteristics and behaviors in a high-speed disperser. Chem. Eng. Sci. 126, 329–340. http://dx.doi.org/10.1016/j.ces.2014.12.049.
Guo, K., Guo, F., Feng, Y.D., Chen, J.F., Zheng, C., Gardner, N.C., 2000. Synchronous visual and RTD study on liquid flow in rotating packed-bed contactor. Chem. Eng. Sci. 55, 1699–1706. http://dx.doi.org/10.1016/S0009-2509(99)00369-3.
Guo, K., Wen, J.W., Zhao, Y., Wang, Y., Zhang, Z.Z., Li, Z.X., Qian, Z., 2014. Optimal packing of a rotating packed bed for H_2S removal. Environ. Sci. Technol. 48, 6844–6849. http://dx.doi.org/10.1021/es404913e.
Guo, T.Y., Shi, X., Chu, G.W., Xiang, Y., Wen, L.X., Chen, J.F., 2016. Computational fluid dynamics analysis of the micromixing efficiency in a rotating-packed-bed reactor. Ind. Eng. Chem. Res. 55, 4856–4866. http://dx.doi.org/10.1021/acs.iecr.6b00213.
Hirt, C.W., Nichols, B.D., 1981. Volume of fluid (Vof) method for the dynamics of free boundaries. J. Comput. Phys. 39, 201–225. http://dx.doi.org/10.1016/0021-9991(81)90145-5.
Jassim, M.S., Rochelle, G., Eimer, D., Ramshaw, C., 2007. Carbon dioxide absorption and desorption in aqueous monoethanolamine solutions in a rotating packed bed. Ind. Eng. Chem. Res. 46, 2823–2833. http://dx.doi.org/10.1021/ie051104r.
Jiao, W.Z., Liu, Y.Z., Qi, G.S., 2010. Gas pressure drop and mass transfer characteristics in a cross-flow rotating packed bed with porous plate packing. Ind. Eng. Chem. Res. 49, 3732–3740. http://dx.doi.org/10.1021/ie9009777.
Joel, A.S., Wang, M.H., Ramshaw, C., 2015. Modelling and simulation of intensified absorber for post-combustion CO_2 capture using different mass transfer correlations. Appl. Therm. Eng. 74, 47–53. http://dx.doi.org/10.1016/j.applthermaleng.2014.02.064.
Joel, A.S., Wang, M.H., Ramshaw, C., Oko, E., 2014. Process analysis of intensified absorber for post-combustion CO_2 capture through modelling and simulation. Int. J. Greenhouse Gas Control 21, 91–100. http://dx.doi.org/10.1016/j.ijggc.2013.12.005.
Kang, J.L., Sun, K., Wong, D.S.H., Jang, S.S., Tan, C.S., 2014. Modeling studies on absorption of CO_2 by monoethanolamine in rotating packed bed. Int. J. Greenhouse Gas Control 25, 141–150. http://dx.doi.org/10.1016/j.ijggc.2014.04.011.
Kang, J.L., Wong, D.S.H., Jang, S.S., Tan, C.S., 2016. A comparison between packed beds and rotating packed beds for CO_2 capture using monoethanolamine and dilute aqueous ammonia solutions. Int. J. Greenhouse Gas Control 46, 228–239. http://dx.doi.org/10.1016/j.ijggc.2016.01.017.
Kumar, M.P., Rao, D.P., 1990. Studies on a high-gravity gas-liquid contactor. Ind. Eng. Chem. Res. 29, 917–920. http://dx.doi.org/10.1021/ie00101a031.
Lan, H., Wegener, J.L., Armaly, B.F., Drallmeier, J.A., 2010. Developing laminar gravity-driven thin liquid film flow down an inclined plane. J. Fluids Eng.–Trans. ASME 132. http://dx.doi.org/10.1115/1.4002109.
Lin, C.C., Chen, Y.S., Liu, H.S., 2000. Prediction of liquid holdup in countercurrent-flow rotating packed bed. Chem. Eng. Res. Des. 78, 397–403. http://dx.doi.org/10.1205/026387600527293.
Lin, C.C., Kuo, Y.W., 2016. Mass transfer performance of rotating packed beds with blade packings in absorption of CO2 into MEA solution. Int. J. Heat Mass Transf. 97, 712–718. http://dx.doi.org/10.1016/j.ijheatmasstransfer.2016.02.033.
Liu, Y., Luo, Y., Chu, G.-W., Luo, J.-Z., Arowo, M., Chen, J.-F., 2017. 3D numerical simulation of a rotating packed bed with structured stainless steel wire mesh packing. Chem. Eng. Sci. http://dx.doi.org/10.1016/j.ces.2017.01.033.
Llerena-Chavez, H., Larachi, F., 2009. Analysis of flow in rotating packed beds via CFD simulations-Dry pressure drop and gas flow maldistribution. Chem. Eng. Sci. 64, 2113–2126. http://dx.doi.org/10.1016/j.ces.2009.01.019.
Menter, F.R., 1994. Two-equation eddy-viscosity turbulence models for engineering applications. AIAA J. 32, 1598–1605. http://dx.doi.org/10.2514/3.12149.
Munjal, S., Dudukovic, M.P., Ramachandran, P., 1989. Mass-transfer in rotating packed beds-I. Development of gas-liquid and liquid-solid mass-transfer correlations. Chem. Eng. Sci. 44, 2245–2256. http://dx.doi.org/10.1016/0009-2509(89)85159-0.
Nikolopoulos, N., Nikas, K.S., Bergeles, G., 2009. A numerical investigation of central binary collision of droplets. Comput. Fluids 38, 1191–1202. http://dx.doi.org/10.1016/j.compfluid.2008.11.007.
Osher, S., Sethian, J.A., 1988. Fronts propagating with curvature-dependent speed – algorithms based on hamilton-jacobi formulations. J. Comput. Phys. 79, 12–49. http://dx.doi.org/10.1016/0021-9991(88)90002-2.
Qian, Z., Xu, L.B., Cao, H.B., Guo, K., 2009. Modeling study on absorption of CO_2 by aqueous solutions of N-methyldiethanolamine in rotating packed bed. Ind. Eng. Chem. Res. 48, 9261–9267. http://dx.doi.org/10.1021/ie900894a.
Ramshaw, C., Mallinson, R.H., 1981. Mass Transfer Process, US Patent No. 4283255.
Raynal, L., Royon-Lebeaud, A., 2007. A multi-scale approach for CFD calculations of gas-liquid flow within large size column equipped with structured packing. Chem. Eng. Sci. 62, 7196–7204. http://dx.doi.org/10.1016/j.ces.2007.08.010.
Saha, D., 2009. Prediction of mass transfer coefficient in rotating bed contactor (Higee) using artificial neural network. Heat Mass Transf. 45, 451–457. http://dx.doi.org/10.1007/s00231-008-0442-0.
Shi, X., Xiang, Y., Wen, L.X., Chen, J.F., 2013. CFD analysis of liquid phase flow in a rotating packed bed reactor. Chem. Eng. J. 228, 1040–1049. http://dx.doi.org/10.1016/j.cej.2013.05.081.
Singh, R.K., Galvin, J.E., Sun, X., 2016. Three-dimensional simulation of rivulet and film flows over an inclined plate: effects of solvent properties and contact angle. Chem. Eng. Sci. 142, 244–257. http://dx.doi.org/10.1016/j.ces.2015.11.029.
Tung, H.H., Mah, R.S.H., 1985. Modeling liquid mass-transfer in Higee separation process. Chem. Eng. Commun. 39, 147–153. http://dx.doi.org/10.1080/00986448508911667.
Wang, M., Joel, A.S., Ramshaw, C., Eimer, D., Musa, N.M., 2015. Process intensification for post-combustion CO_2 capture with chemical absorption: a critical review. Appl. Energy 158, 275–291. http://dx.doi.org/10.1016/j.apenergy.2015.08.083.
Yan, Z.Y., Lin, C., Ruan, Q., 2012. Hydrodynamics in a rotating packed bed. I. A novel experimental method. Ind. Eng. Chem. Res. 51, 10472–10481. http://dx.doi.org/10.1021/ie202257t.
Yan, Z.Y., Lin, C., Ruan, Q., 2014. Dynamics of droplets and mass transfer in a rotating packed bed. AIChE J. 60, 2705–2723. http://dx.doi.org/10.1002/aic.14449.
Yang, W.J., Wang, Y.D., Chen, J.F., Fei, W.Y., 2010. Computational fluid dynamic simulation of fluid flow in a rotating packed bed. Chem. Eng. J. 156, 582–587. http://dx.doi.org/10.1016/j.cej.2009.04.013.
Yang, Y.C., Xiang, Y., Chu, G.W., Zou, H.K., Luo, Y., Arowo, M., Chen, J.F., 2015a. A noninvasive X-ray technique for determination of liquid holdup in a rotating packed bed. Chem. Eng. Sci. 138, 244–255. http://dx.doi.org/10.1016/j.ces.2015.07.044.
Yang, Y.C., Xiang, Y., Chu, G.W., Zou, H.K., Sun, B.C., Arowo, M., Chen, J.F., 2016. CFD modeling of gas-liquid mass transfer process in a rotating packed bed. Chem. Eng. J. 294, 111–121. http://dx.doi.org/10.1016/j.cej.2016.02.054.
Yang, Y.C., Xiang, Y., Li, Y.G., Chu, G.W., Zou, H.K., Arowo, M., Chen, J.F., 2015b. 3D CFD modelling and optimization of single-phase flow in rotating packed beds. Can. J. Chem. Eng. 93, 1138–1148. http://dx.doi.org/10.1002/cjce.22183.
Yi, F., Zou, H.K., Chu, G.W., Shao, L., Chen, J.F., 2009. Modeling and experimental studies on absorption of CO_2 by Benfield solution in rotating packed bed. Chem. Eng. J. 145, 377–384. http://dx.doi.org/10.1016/j.cej.2008.08.004.
Youngs, D.L., 1982. Time-Dependent Multi-Material Flow with Large Fluid Distortion. Academic Press, New York.
Yu, C.-H., Chen, M.-T., Chen, H., Tan, C.-S., 2016. Effects of process configurations for combination of rotating packed bed and packed bed on CO_2 capture. Appl. Energy 175, 269–276. http://dx.doi.org/10.1016/j.apenergy.2016.05.044.
Yuan, Y., Lee, T.R., 2013. Contact Angle and Wetting Properties, Surface Science Techniques. Springer, pp. 3–34. http://dx.doi.org/10.1007/978-3-642-34243-1_1.
Zhang, J.W., Gao, D.X., Li, Y.C., He, J.Y., 2016. Study on micromixing and reaction process in a rotating packed bed. Int. J. Heat Mass Transf. 101, 1063–1074. http://dx.doi.org/10.1016/j.ijheatmasstransfer.2016.05.103.
Zhao, B.T., Su, Y.X., Tao, W.W., 2014. Mass transfer performance of CO_2 capture in rotating packed bed: dimensionless modeling and intelligent prediction. Appl. Energy 136, 132–142. http://dx.doi.org/10.1016/j.apenergy.2014.08.108.
Zheng, X.H., Chu, G.W., Kong, D.J., Luo, Y., Zhang, J.P., Zou, H.K., Zhang, L.L., Chen, J.F., 2016. Mass transfer intensification in a rotating packed bed with surface-modified nickel foam packing. Chem. Eng. J. 285, 236–242. http://dx.doi.org/10.1016/j.cej.2015.09.083.